RESEARCH ARTICLE

National Science Review
0: nwab066, 2021
https://doi.org/10.1093/nsr/nwab066
Advance access publication 20 April 2021

MATERIALS SCIENCE

ZnO-based micromotors fueled by CO_2: the first example of self-reorientation-induced biomimetic chemotaxis

Fangzhi Mou†, Qi Xie†, Jianfeng Liu, Shengping Che, Lamya Bahmane, Ming You and Jianguo Guan*

ABSTRACT

Synthetic chemotactic micro/nanomotors are envisioned to actively 'seek out' targets by following specific chemicals, but they are mainly powered by bioincompatible fuels and only show pseudochemotaxis (or advanced chemokinesis) due to their weak self-reorientation capabilities. Here we demonstrate that synthetic ZnO-based Janus micromotors can be powered by the alternative biocompatible fuel of CO_2, and further provide the first example of self-reorientation-induced biomimetic chemotaxis using them. The ZnO-based micromotors are highly sensitive to dissolved CO_2 in water, which enables the corrosion of ZnO to continuously occur by providing H^+ through hydration. Thus, they can autonomously move even in water exposed to air based on self-diffusiophoresis. Furthermore, they can sense the local CO_2 gradient and perform positive chemotaxis by self-reorientations under the phoretic torque. Our discovery opens a gate to developing intelligent micro/nanomotors powered by, and sensitive to, biocompatible atmospheric or endogenous gaseous chemicals for biomedical and environmental applications.

Keywords: micro/nanomotors, zinc oxide, carbon dioxide, self-propulsion, chemotaxis

State Key Laboratory of Advanced Technology for Materials Synthesis and Processing, International School of Materials Science and Engineering, Wuhan University of Technology, Wuhan 430070, China

*Corresponding author. E-mail: guanjg@whut.edu.cn
†Equally contributed to this work.

Received 8 December 2020; **Revised** 8 March 2021; **Accepted** 11 April 2021

INTRODUCTION

Biological chemotaxis refers to the ability of those living organisms that are of an advanced level of evolution to move toward or away from specific chemicals [1,2]. To achieve chemotaxis, the living organisms are equipped with delicately coordinated sensing, signal processing and propelling systems, endowing them with the capability to adjust their motion direction on demand by evaluating the direction of chemical gradients at different times (e.g. the temporal comparison adopted by *Escherichia coli*) or perceiving signal intensity differences across their body (e.g. the spatial comparison adopted by neutrophils) [3,4]. Chemotaxis not only regulates the development of multicellular systems such as tissue development and cancer metastasis, but also enables many unicellular organisms to find nourishments, avoid toxins and coordinate collective motions [5–7].

Inspired by biological chemotaxis, researchers strive to create synthetic chemotactic micro/nanomotors (MNMs). They are envisioned to achieve self-navigation and self-targeting in complex or dynamic environments by actively following specific chemical cues, and thus may bring revolutionary changes to targeted drug delivery, microsurgeries, microfactories, etc [8]. Nonetheless, synthetic MNMs are generally too small to incorporate sophisticated sensing-processing-propelling systems and have a low sensitivity to chemical gradients. Thus, they only show a pseudochemotaxis (or macroscopic chemotaxis and advanced chemokinesis) based on a purely statistical effect rather than chemotaxis of individual MNMs because of the stochastic nature in motion for each individual [8,9]. With the pseudochemotaxis, they show negligible reorientation capabilities, and can only accumulate near (or away from) the chemoattractant (or chemorepellent) source, or shift toward (or away from) its stream in microfluidic channels due to their spatial-dependent mobility (orthokinesis) in the local chemical gradient field [8,10–13]. This statistically average movement uphill (or downhill) to a chemical gradient based on orthokinesis undermines the self-targeting performance of MNMs, and is far from the biological chemotaxis found in

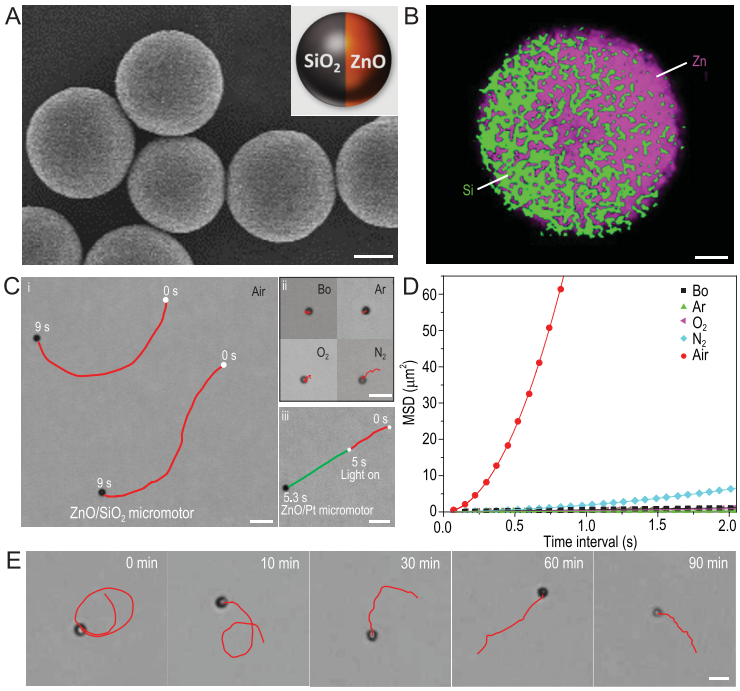

Figure 1. Characterization and self-propulsions of the ZnO-based MMs. (A) SEM image of the ZnO/SiO_2 MMs. Scale bar, 1 μm. The inset shows the schematic illustration of their Janus structure. (B) EDX mapping of Zn and Si elements in a ZnO/SiO_2 MM. Scale bar, 500 nm. (C) Self-propulsions of ZnO-based MMs in different water media. (i and ii) Trajectories of ZnO/SiO_2 MMs in 9 s in the (i) air-exposed water (Air) and (ii) CO_2-eliminated water, including the freshly boiled water (Bo), Ar-gassed water (Ar), O_2-gassed water (O_2) and N_2-gassed water (N_2). Scale bars, 10 μm. (iii) Trajectories of a ZnO/Pt MM in the air-exposed water without (red curve) and with (green curve) UV irradiation. Scale bars, 5 μm. (D) MSD of the MMs in different water media. Solid color lines are fitting curves using a quadratic function. (E) Self-propulsion of a typical ZnO/SiO_2 MM within a lifetime of 90 min. Red curves depict its trajectories in 9 s at different time intervals. Scale bar, 5 μm.

nature. On the other hand, chemically powered MNMs have been predicted, in theory, to achieve chemotaxis through their self-reorientation based on the spatial comparison of chemical signal intensity across their bodies, like neutrophils [14,15], but it has not been experimentally confirmed.

In this work, we demonstrate ZnO-based Janus micromotors (MMs) powered by an alternative fuel of CO_2, and further provide the first example of self-reorientation-induced biomimetic chemotaxis using them. The ZnO-based MMs can autonomously move based on electrolyte self-diffusiophoresis, even in water exposed to air, as the ZnO component in the MMs is highly sensitive to CO_2 dissolved in water, which continuously produces H^+ through hydration to react with ZnO. In this way, the MMs can sense local CO_2 signals, and exhibit a biomimetic chemotactic behavior toward the CO_2 source due to their dynamic reorientations under a phoretic torque. The proposed alternative fuel of CO_2, which is a constituent gas in the air and a major product of cell respiration [16,17], has remarkable advantages, including sustained remote accessibility, low cost and excellent biocompatibility. With the excellent biomedical activities of ZnO [18], the intelligent chemotactic behaviors promise that the ZnO-based MMs will 'seek out' specific cells or pathogen microorganisms by tracking metabolic CO_2 signals emitted from them, and execute targeted biomedical and environmental operations.

RESULTS AND DISCUSSION

To experimentally achieve the biomimetic chemotaxis of artificial MNMs, we at first prepared ZnO-based MMs by sputtering a thin layer of SiO_2 on the exposed surface of hexagonal wurtzite ZnO microspheres (Supplementary Fig. 1A and B), as illustrated in Supplementary Fig. 2. The scanning electron microscope (SEM) observation indicates that the prepared ZnO/SiO_2 MMs have a relatively uniform spherical shape and an average diameter (d) of 2.5 μm (Fig. 1A). Energy dispersive X-ray (EDX) mapping of Zn and Si elements confirms that the ZnO/SiO_2 MMs have a typical Janus structure (the inset in Fig. 1A, and Fig. 1B). The thickness of the sputtered SiO_2 layer is ~150 nm, as verified by the high-contrast SEM observation (Supplementary Fig. 3A) and line-scanning EDX analysis of Zn and Si elements (Supplementary Fig. 3B) on a typical ZnO/SiO_2 MM. Zeta potential test shows that the ZnO microspheres before and after coating SiO_2 have a similar negative surface charge of 24.1 and −23.7 mV, respectively.

When the ZnO/SiO_2 MMs were put into water previously exposed to air (air-exposed water, see 'Materials' section in the online Supplementary Data), they exhibited an autonomous motion with an average speed (v) of 7.8 μm/s (Fig. 1C(i) and Supplementary Video 1). As ZnO is poorly reactive or soluble in pure water [19], the self-propulsion of the MMs was attributed to atmospheric CO_2 because it has a much higher solubility (34 mM at 25°C and 1 atm) in water compared to other major constituent gases (such as N_2, O_2 and Ar) [20]. To confirm the key role of CO_2 in the self-propulsion of the ZnO/SiO_2 MMs, we investigated their motions in CO_2-eliminated water (see 'Materials' section in the online Supplementary Data), including freshly boiled water (pH = 7.54), Ar-gassed water (pH = 7.46), O_2-gassed water (pH = 7.36) and N_2-gassed water (pH = 6.67), respectively (Supplementary Video 1). As shown in Fig. 1C(ii) and D, they show an extremely slow motion in the N_2-gassed water and only Brownian motions

in other CO_2-eliminated water, with a translational v and diffusivity (D) lower than 1.3 μm/s and 0.14 $\mu m^2/s$, respectively. The translational v and D were extracted by fitting their mean square displacements (MSDs, Fig. 1D) using a quadratic function according to the previous report [21].

The SiO_2 cap on the ZnO/SiO_2 MMs only acts as a passive layer to break the symmetry of the surface reaction of ZnO. This can be verified by the fact that the ZnO microspheres only exhibit Brownian motions in the air-exposed water due to isotropic surface reactions (Supplementary Fig. 4), and the MM can still be self-propelled in the same condition if the SiO_2 cap is replaced by a Pt cap (Fig. 1C(iii)). The ZnO/SiO_2 MMs showed similar motions in low-energy red light (20.2 mW/cm^2) and high-energy UV light (300 mW/cm^2) (Supplementary Fig. 5), while the ZnO/Pt MMs were accelerated under the irradiation of UV light because of their high photocatalytic activity (Supplementary Video 2 and Fig. 1C(iii)). This suggests that light illumination has a negligible contribution to the self-propulsion of ZnO/SiO_2 MMs. Air-exposed water has a CO_2 concentration (C_{CO_2}) of 8.54 μM (pH = 5.72), which is three orders lower than the critical concentration of the H_2O_2 fuel (~60 mM) required to power traditional catalytic Pt-based MNMs [22]. This suggests that the MMs are highly sensitive to dissolved CO_2 in water and can be powered at an ultralow level of the chemical fuel. Moreover, the ZnO/SiO_2 MMs exhibit a long lifetime of ~90 min (Fig. 1E), which is higher than that of the active metal-based MMs (~5 min), catalytic MnO_2 MMs (≤40 min) and some enzyme-based MMs (≤40 min) [23–25].

CO_2 exists as a stable and inert gas in air, but can remotely diffuse into various aqueous media to participate in a number of reactions after hydration, such as acidic corrosion [17,26–29]. In detail, when water is exposed to air, CO_2 molecules, which account for ~0.04% of the air in volume [30], can enter into the water through the interface with the atmosphere, and are partially hydrated into H_2CO_3, which then dissociates into HCO_3^- and H^+, as described by equation (1) [31]:

$$CO_2 + H_2O \leftrightharpoons H_2CO_3 \leftrightharpoons H^+ + HCO_3^-. \quad (1)$$

Afterwards, the ZnO-based MMs react with the released H^+ according to equation (2) [19]:

$$2H^+ + ZnO \rightarrow Zn^{2+} + H_2O. \quad (2)$$

The acidity constant (K_a) of the dissolved CO_2 molecules is 4.3×10^{-7} M at room temperature, indicating that only a small amount of them are converted into H^+ and HCO_3^-. In this way, the dissolved CO_2 stayed as molecules can continuously supply H^+ ions through the local equilibrium reaction (equation (1)) when H^+ is consumed by ZnO, and thus CO_2 is considered as the chemical fuel powering the ZnO-based MMs according to an overall reaction expressed as equation (3):

$$ZnO + 2CO_2 + H_2O \rightarrow Zn^{2+} + 2HCO_3^-. \quad (3)$$

Due to the different D of the released ionic products of HCO_3^- ($D = 1.185 \times 10^{-9}$ m^2/s) and Zn^{2+} ($D = 0.703 \times 10^{-9}$ m^2/s) from the ZnO/SiO_2 MMs according to equation (3), HCO_3^- would diffuse faster than Zn^{2+} [32,33], leading to an uneven distribution of these ions in the area near the exposed ZnO surface (Supplementary Fig. 6A and B). To maintain electroneutrality, a local diffusioelectric field (E) arises to slow down the faster-diffusing ion, and speed up the slower ion [34], as verified by the simulated electric potential φ depicted in the color background of Fig. 2A and the local E shown in Supplementary Fig. 6C (black triangles). This local E then induces an electro-osmotic slip (EOS) [35] in the electric double layer of the negatively charged MM ($\zeta = -23.7$ mV). The simulated flow field (EOF) initiated by the surface EOS around a ZnO/SiO_2 MM is illustrated as black streamlines with arrows in Fig. 2A, revealing that the MMs are self-propelled based on electrolyte self-diffusiophoresis with the ZnO end forward. This propulsion direction was further experimentally verified by the close observation of a partially etched ZnO/SiO_2 MM and the barely etched SiO_2/ZnO MMs, both of which have a distinguishable ZnO end at a high magnification under an optical microscope (Supplementary Figs 7 and 8, Supplementary Video 3). The detailed propulsion mechanism of the ZnO/SiO_2 MM fueled by the dissolved atmospheric CO_2 in water is illustrated in Fig. 2B.

From the propulsion mechanism (Fig. 2B), it is expected that the ZnO-based MMs can still acquire fuel from the air even if no CO_2 was pre-dissolved in water. To verify this assumption, we recorded the motion behaviors of the ZnO/SiO_2 MMs in a thin film (~160 μm in thickness) of the freshly boiled water over time when exposed to air (Fig. 2C and Supplementary Video 4). Differently to the MMs in the air-exposed water film ($C_{CO_2} = 8.54$ μM), which show a decreasing v over time (the black curve with dots in Fig. 2D), those in the CO_2-eliminated water display an increasing v in the first 7 min (the red curve with dots in Fig. 2D). This behavior can be verified by the different lengths of trajectories of a typical MM in 8 s (Fig. 2C) and the statistic normalized v of the MMs (Fig. 2D) at different intervals within 7 min. This increase in v reveals

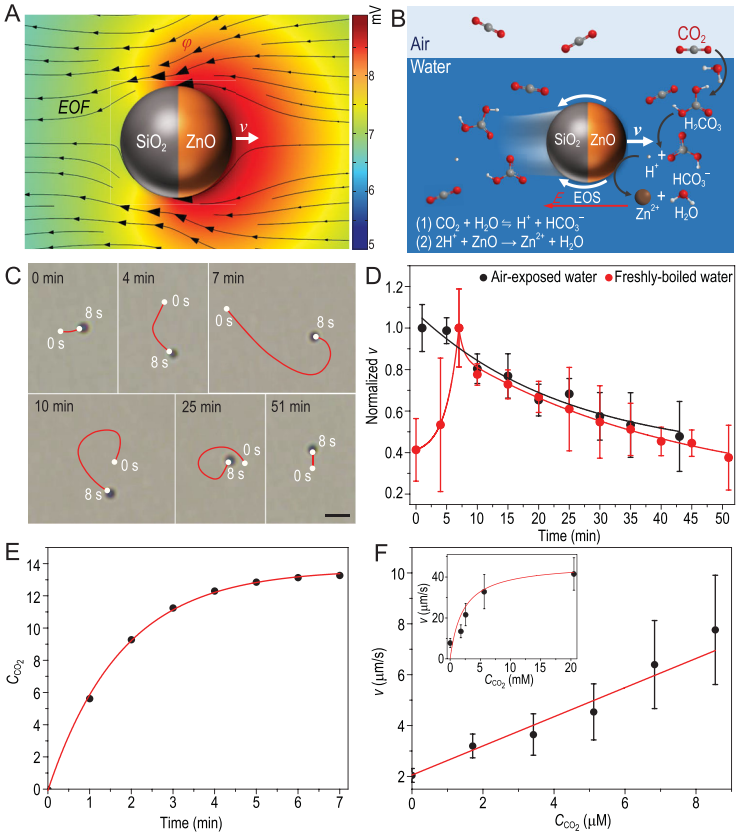

Figure 2. The self-propulsion mechanism of the ZnO/SiO_2 MMs. (A) Numerical simulations of the electric potential (φ, the color background) and the electro-osmotic flow (EOF, black streamlines with arrows) around a ZnO/SiO_2 MM. The EOF is initiated by the surface electro-osmotic slip (EOS) in its electric double layer. (B) Schematic illustration of the propulsion mechanism of the ZnO/SiO_2 MMs. (C) Trajectories of the MMs in freshly boiled water at different time intervals when exposed to air. Scale bar, 5 μm. (D) Time-dependent normalized v of the MMs in a film of freshly boiled water when exposed to air (red dots) and the air-exposed water (black dots). Solid red and black curves are fitting results using exponential functions. (E) The simulated C_{CO_2} as a function of time in a CO_2-eliminated water film (160 μm in thickness) when exposed to air. (F) The v of the MMs at different C_{CO_2} in water. The red line is the linear fitting line of the experimental data in the low C_{CO_2} regime (0–8.54 μM), and the red curve in the inset is the fitting result according to the Michaelis-Menten kinetics in the high C_{CO_2} regime (8.54 μM to 20.5 mM).

that atmospheric CO_2 molecules can diffuse into the water as fuel to power the MMs in a sustainable and rapid manner, as verified by the numerical results of the increasing C_{CO_2} (Fig. 2E and Supplementary Fig. 9A) and H^+ concentration (C_{H^+}, Supplementary Fig. 9B) over time when the water film is exposed to air. In the following 7–51 min, the v of the MMs decreases gradually due to the decreasing reaction rate of ZnO and the increasing ion concentration in the water film. With the increase of C_{CO_2} from 0 to 8.54 μM, the v of the ZnO/SiO_2 MMs increases from 2.0 to 7.8 μm/s (Fig. 2F and Supplementary Video 5). By bubbling water with pure CO_2 gas, a higher C_{CO_2} compared to that in the air-exposed water can be obtained, and the v of MMs can reach 41.5 μm/s when C_{CO_2} increases to 20.5 mM (the inset in Fig. 2F and Supplementary Video 5). The fitting results show that the v of the MMs increases linearly in the low C_{CO_2} regime from 0 to 8.54 μM (red line in Fig. 2F), and gradually reaches to a plateau in the high C_{CO_2} regime (8.54 μM–20.5 mM) following Michaelis-Menten kinetics (red curve in the inset of Fig. 2F). These results reveal that the ZnO/SiO_2 MMs are of a high sensitivity to C_{CO2}, especially in the low C_{CO_2} regime. The sensitivity can be quantified by the rate of the speed change of the ZnO/SiO_2 MMs to C_{CO_2}, which has a value of 0.57 μm/(μM·s) (the slope of the red line in Fig. 2F) in the low C_{CO_2} regime, about five orders of magnitude higher than that of common H_2O_2-fueled MMs (2.72×10^{-6} μm/(μM·s)) [36]. The appearance of the plateau of v at a high C_{CO_2} of 20.5 mM indicates that the maximum speed is limited by the maximum reaction rate depending on total surface reactive sites.

Benefiting from the high sensitivity to C_{CO_2}, the ZnO/SiO_2 MMs can sense a local CO_2 gradient and exhibit positive chemotaxis toward a local CO_2 source in water (Fig. 3A). When a micropipette filled with a CO_2 solution ($C_{CO2} = 93.7$ μM) was introduced to the water medium ($C_{CO_2} = 0.2$ μM), a gradient field of C_{CO_2} (∇C) is formed (the color background in Fig. 3A). In this gradient field, the ZnO/SiO_2 MMs swarm toward the micropipette, in analogy to the positive chemotaxis of living organisms in nature (Fig. 3B and Supplementary Video 6). The average chemotactic velocity, defined as the net displacement of the ZnO/SiO_2 MMs divided by time when they are approaching the region close to (~20 μm) the CO_2 source, is 0.57 μm/s. In contrast, passive SiO_2 microspheres ($d = 2$ μm and $\zeta = -18.5$ mV) show no chemotactic motion in the same gradient field (Supplementary Fig. 10 and Supplementary Video 7), indicating that the MMs were actively swimming toward the CO_2 source, and the possible passive diffusiophoretic attraction generated by the gradient field is negligible.

To quantify the degree of chemotaxis, we have analyzed the chemotaxis index (CI) of ZnO/SiO_2 MMs, which was defined as the ratio of the displacement in the direction of the chemical gradient to the total migration distance (i.e. as the cosine of the angle θ of the MM's motion direction with the chemical gradient) [37]. The average CI is 0.21, suggesting that they, in general, move uphill to the chemical gradient. Due to the persistent ZnO-forward configurations during the propulsion (Supplementary Figs 6 and 7), the self-reorientation dynamics of the ZnO/SiO_2 MMs can be characterized by the changes of CI and the angle θ over time. When $CI > 0$ (i.e. $0 \leq |\theta| < \pi/2$), the ZnO/SiO_2 MMs

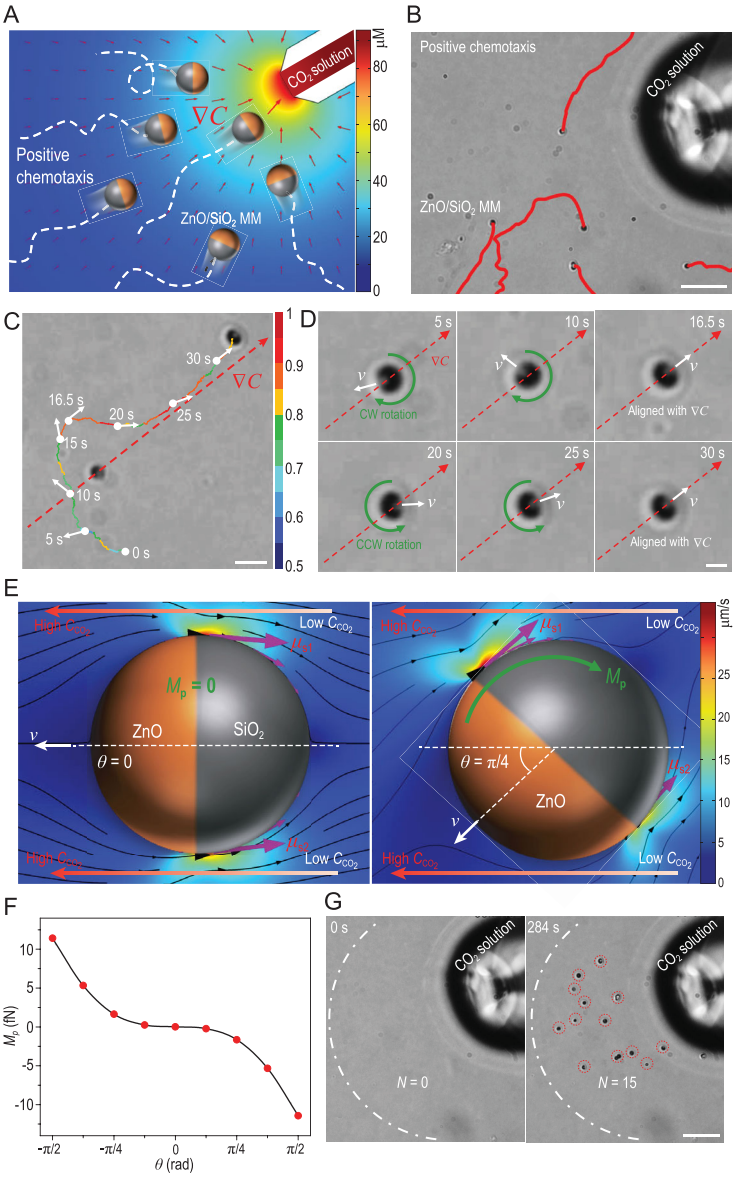

Figure 3. Chemotaxis of the ZnO/SiO_2 MMs. (A) Schematic illustration of the positive chemotaxis of the ZnO/SiO_2 MMs. The color background depicts numerical simulations of C_{CO_2} gradient (∇C) near a micropipette (inner d, 20 μm) filled with a CO_2 solution (C_{CO_2} = 93.7 μM). (B) Trajectories of the MMs moving toward the CO_2 source. Scale bar, 20 μm. (C) The color trajectory of a slightly etched ZnO/SiO_2 MM approaching the CO_2 source, in which the colors represent the normalized magnitude of v of the MM. Scale bar, 5 μm. (D) The reorientations of the ZnO/SiO_2 MM shown in (C) at different times by clockwise (CW) or counterclockwise (CCW) rotations. Scale bar, 2 μm. (E) Numerical simulations of the EOSs (purple arrows) on a ZnO/SiO_2 MM and the resulted flow fields (black streamlines with black arrows) when it aligns with ∇C (θ = 0, the left panel) and deviates with it in a θ of π/4 (the right panel), respectively. The color background depicts the magnitude of the flow velocity. The green arrow represents the phoretic torque (M_p) induced by the unbalanced EOSs. (F) The calculated M_p at different θ. (G) Time-lapse images displaying the change of N near the CO_2 source. Scale bar, 20 μm.

prefer to move up the gradient, while they tend to move down the gradient if $CI < 0$ (i.e. $\pi/2 < |\theta| \leq \pi$). The CI and $|\theta|$ of four typical ZnO/SiO_2 MMs versus time (Supplementary Fig. 11) suggest that they move up the gradient for a longer time than moving down. The longer upgradient motion time implies that the ZnO/SiO_2 MMs prefer to move with an orientation along the upgradient direction even though their motion direction was seriously randomized by the Brownian rotational diffusions.

To further demonstrate the biomimetic chemotactic behavior, the instantaneous v, orientation and rotation of a slightly etched ZnO/SiO_2 MM, in which the slightly etched ZnO end was distinguishable under an optical microscope, were recorded and analyzed when it was approaching the CO_2 source (Fig. 3C and D). The ZnO/SiO_2 MM shows an increasing v when approaching the CO_2 source because of the increasing C_{CO_2} (i.e. orthokinesis of the motor [38]), as verified by the normalized instantaneous v in 0–15 s and 15–30 s (Fig. 3C), respectively. In addition, when the ZnO/SiO_2 MM deviates with ∇C because of the strong perturbations of Brownian randomizations, it dynamically reorientates itself by clockwise or counterclockwise rotations (Fig. 3D). When the MM moves with an orientation down ∇C, it rotates clockwise gradually and aligns with ∇C (0–16.5s in Fig. 3D). After a sharp turn (16.5–20 s in Fig. 3D), the MM deviates with ∇C again, and then gradually aligns with ∇C by a counterclockwise rotation (20–30 s in Fig. 3D). This self-reorientation behavior bears resemblance to that of chemotactic microorganisms which show a 'memory' of the direction of the chemical gradient and move up the gradient of chemoattractant in a 'deviating-rectifying' manner. This is the first experimental evidence showing that synthetic MNMs can achieve chemotaxis by dynamic self-reorientations in a gradient field [8]. After reaching the area close to the tip of the micropipette (CO_2 source), the MMs were wandering in this area with no preferred directions, as depicted by the curved trajectory of the slightly etched MM in 34–163 s in Supplementary Fig. 12, so that they could accumulate near the CO_2 source (Supplementary Video 6).

To decipher the chemotactic behavior, we have simulated the flow field around the ZnO-based MM when a local CO_2 source is introduced, as shown in Fig. 3E. The results show that, if the axis of the MM is aligned with the CO_2 gradient, EOSs (e.g. u_{s1} and u_{s2} in the left panel in Fig. 3E, $u_{s1} = u_{s2}$) across the axis of the MM are symmetrical because of symmetric surface reactions, and the MM migrates up the gradient at this condition. However, due to the strong rotational Brownian diffusion, the symmetry axis of the MM is constantly deviating from ∇C. When misaligned with ∇C with an angle of θ, the ZnO surface close to the CO_2 source has a higher reaction rate (due to the higher C_{CO_2} (or C_{H^+})) than the surface further away from the source, resulting in the asymmetric distribution of chemical

products and thus unbalanced EOSs across the motor axis (e.g. u_{s1} and u_{s2} in the right panel of Fig. 3E, $u_{s1} > u_{s2}$). The unbalanced EOSs then produce a phoretic torque (M_p) to induce rotation of the MM until its axis is aligned with ∇C (the right panel of Fig. 3E). With the increasing degree of deviation, the self-EOSs across the motor axis become more unbalanced, and thus M_p increases accordingly for reorientation, as verified by the increasing M_p with a varying θ from 0 to $-\pi/2$ and $\pi/2$ (Fig. 3F). Hence, the chemotactic behavior of the MM is attributed to dynamic self-reorientations under the phoretic torque. Due to their self-reorientations, they show a higher efficiency in chemotaxis compared to the developed (pseudo)chemotactic MNMs, which usually take hours to aggregate near the chemical source [10,39,40]. As shown in Fig. 3G, the MMs swarm to the chemical source in several minutes, as demonstrated by the increasing number (N) of MMs from 0 to 15 within 284 s in a sector region close to (80 μm) the CO_2 source.

CO_2 not only exists in the air and various aqueous media (such as natural waters and biological media), but also can be produced and secreted by cells or pathogenic microorganisms during their oxidative metabolism [41–44]. For instance, the CO_2 tension (P_{CO_2}) of the intracellular and extracellular fluids is ∼50 and 46 mmHg, indicating that there is a high C_{CO_2} (∼20.8 and 19.3 mM together with the chemically bound CO_2) and a steep C_{CO_2} gradient near tissue cells (e.g. $\sim 3.3 \times 10^4$ mol/m^4 at a distance of 20 μm to the cell surface), respectively [45]. On the other hand, ZnO micro/nanomaterials are of low toxicity and good biodegradability and have shown great potential in biomedical applications due to their excellent anti-cancer, anti-diabetic, anti-bacterial and anti-inflammatory activities [18]. Thus, the chemotactic ZnO-based MMs with proper surface modifications (e.g. polyelectrolyte ion-tolerance coating [46]) are expected to act as biomimetic microrobots, 'seeking out' specific cells or pathogenic microorganisms by actively tracking their extracellular CO_2 signals, thereby executing targeted biomedical and environmental operations.

CONCLUSION

In conclusion, we have demonstrated that ZnO-based MMs can be powered by CO_2 fuels and perform intelligent positive chemotaxis by self-reorientations. We analyzed the propulsion mechanism of ZnO-based MMs and confirmed that it was the result of electrolyte self-diffusiophoresis based on the corrosion of the ZnO end by H^+ continuously supplied from the dissolved CO_2. Benefiting from their high sensitivity to local CO_2 signals, the ZnO-based MMs can perform a biomimetic chemotactic behavior toward the CO_2 source due to their dynamic self-reorientations in the chemical gradient field. The self-reorientation of the MM is attributed to the phoretic torque produced by the unbalanced EOSs across the MM axis when it is misaligned with the chemical gradient. Due to the readily accessible biocompatible CO_2 fuel and intelligent chemotaxis, ZnO-based MMs have the potential to autonomously move in a wide range of aqueous media and execute targeted biomedical and environmental operations by actively tracking respiratory CO_2 signals emitted from cells or pathogenic microorganisms.

METHODS

Preparation of ZnO-based MMs

The ZnO microspheres were synthesized according to the previous report [47]. To prepare ZnO/SiO_2 MMs, the ZnO microspheres on the glass slide were partially coated with a SiO_2 nanolayer by magnetron sputtering for 40 min (JCP500, Beijing Technol Science Co., Ltd, China). The substrate was heated to 100°C and rotated at a speed of 30 r/min during the sputtering process. In addition, ZnO/Pt MMs and SiO_2/ZnO MMs were also prepared by sputtering Pt on the ZnO microspheres on the glass slide for 30 s and a ZnO layer on monodispersed SiO_2 microspheres (2 μm) for 60 min, respectively.

Self-propulsion and chemotaxis

To observe the self-propulsion of ZnO/SiO_2 MMs, a 20 μL aqueous suspension of the MMs (0.03 mg/mL) was dropped into a Petri dish (d = 35 mm) with 2 ml water. The self-propulsion of the MMs was observed and recorded through an inverted optical microscope (Leica DMI 3000B). All videos were analyzed using ImageJ and Video Spot Tracker V08.01 software. More than 10 MMs were analyzed to obtain the statistical result. To investigate the MM's chemotaxis, a micropipette (inner d, 20 μm) filled with a CO_2 solution (C_{CO_2} = 93.7 μM) was fixed on the holder of a high-precision micromanipulator (Leica Microsystems, Germany) and then put in a water droplet (50 μL, pH = 6.52) with the ZnO/SiO_2 MMs (0.003 mg/mL).

Numerical simulations

The simulations were performed by using the diffusions, electrostatics and creeping flow modules of

COMSOL Multiphysics software [21]. Governing equations for numerical simulations are given in the online Supplementary Data. The simulation model was built up by immersing a ZnO/SiO_2 MM in the middle of a cylindric cell (radius $r = 50\ \mu$m, height $h = 100\ \mu$m) filled with the air-exposed water ($C_{CO_2} = 8.54\ \mu$M). The fluxes (J) of Zn^{2+}, H^+ and HCO_3^- from the ZnO surface were set as 0.05, -0.1 and 0.1 mmol m^{-2} s^{-1}, respectively. The D of Zn^{2+}, CO_2, H^+ and HCO_3^- were set as 0.70×10^{-9}, 1.77×10^{-9}, 9.31×10^{-9} and 1.19×10^{-9} m^2/s, respectively. The ζ of the MM was set as -23.7 mV. To simulate the reorientation of the MM during chemotaxis, a CO_2 source ($C_{CO_2} = 93.7\ \mu$M) was added in the above model and placed at the left boundary with an r of 10 μm and a distance of 50 μm to the center, and J of Zn^{2+} and HCO_3^- at each point of the exposed ZnO surface was set to be proportional to the local C_{H^+}. To simulate the diffusion kinetics of atmospheric CO_2 (0.04 vol.% in the air) into water through the interface with the atmosphere, a simulation model of a water film (160 μm in thickness) was built and the classical two-film theory was used [48], in which the mass transfer coefficient (k) of CO_2 in the water was set to be 2 μm/s [49], and the equilibrium concentration (C^*) of CO_2 at the interface was calculated to be 1.2×10^{-5} M according to Henry's Law equation.

SUPPLEMENTARY DATA

Supplementary data are available at *NSR* online.

ACKNOWLEDGEMENTS

The authors acknowledge Mr Kong Xiong, Dr Leilei Xu and Dr Ming Luo for their valuable discussion on the manuscript.

FUNDING

This work was supported by the National Natural Science Foundation of China (52073222, 21875175, 21975195, 21705123 and 51521001), the Natural Science Foundation of Hubei Province (2019CFA048), and the Fundamental Research Funds for the Central Universities (WUT: 2021IVA118).

AUTHOR CONTRIBUTIONS

F.M. and J.G. proposed and supervised the project. F.M. conceived and designed the experiments. F.M., Q.X., J.L. and M.Y. carried out the synthesis, structural characterization and self-propulsion tests. F.M. and S.C. carried out theoretical calculations and numerical simulations. F.M., Q.X., J.L., L.B. and J.G. co-wrote the manuscript. All authors discussed the results and participated in analyzing the experimental results.

Conflict of interest statement. None declared.

REFERENCES

1. Parent CA and Devreotes PN. A cell's sense of direction. *Science* 1999; **284**: 765–70.
2. Vorotnikov AV. Chemotaxis: movement, direction, control. *Biochemistry* 2011; **76**: 1528–55.
3. Sourjik V. Receptor clustering and signal processing in *E. coli* chemotaxis. *Trends Microbiol* 2004; **12**: 569–76.
4. Kay RR, Langridge P and Traynor D *et al.* Changing directions in the study of chemotaxis. *Nat Rev Mol Cell Bio* 2008; **9**: 455–63.
5. Porter SL, Wadhams GH and Armitage JP. Signal processing in complex chemotaxis pathways. *Nat Rev Microbiol* 2011; **9**: 153–65.
6. Zou Y-R, Kottmann AH and Kuroda M *et al.* Function of the chemokine receptor CXCR4 in haematopoiesis and in cerebellar development. *Nature* 1998; **393**: 595–9.
7. Roussos ET, Condeelis JS and Patsialou A. Chemotaxis in cancer. *Nat Rev Cancer* 2011; **11**: 573–87.
8. Plutnar J and Pumera M. Chemotactic micro- and nanodevices. *Angew Chem Int Ed* 2019; **58**: 2190–6.
9. Tu Y, Peng F and Wilson DA. Motion manipulation of micro- and nanomotors. *Adv Mater* 2017; **29**: 1701970.
10. Hong Y, Blackman NMK and Kopp ND *et al.* Chemotaxis of nonbiological colloidal rods. *Phys Rev Lett* 2007; **99**: 178103.
11. Baraban L, Harazim SM and Sanchez S *et al.* Chemotactic behavior of catalytic motors in microfluidic channels. *Angew Chem Int Ed* 2013; **52**: 5552–6.
12. Somasundar A, Ghosh S and Mohajerani F *et al.* Positive and negative chemotaxis of enzyme-coated liposome motors. *Nat Nanotechnol* 2019; **14**: 1129–34.
13. Joseph A, Contini C and Cecchin D *et al.* Chemotactic synthetic vesicles: design and applications in blood-brain barrier crossing. *Sci Adv* 2017; **3**: e1700362.
14. You M, Chen C and Xu L *et al.* Intelligent micro/nanomotors with taxis. *Accounts Chem Res* 2018; **51**: 3006–14.
15. Popescu MN, Uspal WE and Bechinger C *et al.* Chemotaxis of active Janus nanoparticles. *Nano Lett* 2018; **18**: 5345–9.
16. Cherniack NS and Longobardo GS. Oxygen and carbon dioxide gas stores of the body. *Physiol Rev* 1970; **50**: 196–243.
17. Geers C and Gros G. Carbon dioxide transport and carbonic anhydrase in blood and muscle. *Physiol Rev* 2000; **80**: 681–715.
18. Mishra PK, Mishra H and Ekielski A *et al.* Zinc oxide nanoparticles: a promising nanomaterial for biomedical applications. *Drug Discov Today* 2017; **22**: 1825–34.
19. Zhou J, Xu NS and Wang ZL. Dissolving behavior and stability of ZnO wires in biofluids: a study on biodegradability and biocompatibility of ZnO nanostructures. *Adv Mater* 2006; **18**: 2432–5.

20. Wilhelm E, Battino R and Wilcock RJ. Low-pressure solubility of gases in liquid water. *Chem Rev* 1977; **77**: 219–62.
21. Jang B, Wang W and Wiget S *et al.* Catalytic locomotion of core-shell nanowire motors. *ACS Nano* 2016; **10**: 9983–91.
22. Gao W, Pei A and Dong R *et al.* Catalytic iridium-based Janus micromotors powered by ultralow levels of chemical fuels. *J Am Chem Soc* 2014; **136**: 2276–9.
23. Wei X, Beltrán-Gastélum M and Karshalev E *et al.* Biomimetic micromotor enables active delivery of antigens for oral vaccination. *Nano Lett* 2019; **19**: 1914–21.
24. Safdar M, Wani OM and Jänis J. Manganese oxide-based chemically powered micromotors. *ACS Appl Mater Interfaces* 2015; **7**: 25580–5.
25. Wang L, Hortelão AC and Huang X *et al.* Lipase-powered mesoporous silica nanomotors for triglyceride degradation. *Angew Chem Int Ed* 2019; **58**: 7992–6.
26. Giordano M, Beardall J and Raven JA. CO_2 concentrating mechanisms in algae: mechanisms, environmental modulation, and evolution. *Annu Rev Plant Biol* 2005; **56**: 99–131.
27. Peng C, Crawshaw JP and Maitland GC *et al.* Kinetics of calcite dissolution in CO_2-saturated water at temperatures between (323 and 373) K and pressures up to 13.8 MPa. *Chem Geol* 2015; **403**: 74–85.
28. Xie S, Zhang Q and Liu G *et al.* Photocatalytic and photoelectrocatalytic reduction of CO_2 using heterogeneous catalysts with controlled nanostructures. *Chem Commun* 2016; **52**: 35–59.
29. Kermani MB and Morshed A. Carbon dioxide corrosion in oil and gas production—a compendium. *Corrosion* 2003; **59**: 659–83.
30. Knohl A and Veldkamp E. Indirect feedbacks to rising CO_2. *Nature* 2011; **475**: 177–8.
31. Loerting T and Bernard J. Aqueous carbonic acid (H_2CO_3). *ChemPhysChem* 2010; **11**: 2305–9.
32. Zeebe RE. On the molecular diffusion coefficients of dissolved CO_2, HCO_3^-, and CO_3^{2-} and their dependence on isotopic mass. *Geochim Cosmochim Acta* 2011; **75**: 2483–98.
33. Mou F, Li X and Xie Q *et al.* Active micromotor systems built from passive particles with biomimetic predator–prey interactions. *ACS Nano* 2020; **14**: 406–14.
34. Velegol D, Garg A and Guha R *et al.* Origins of concentration gradients for diffusiophoresis. *Soft Matter* 2016; **12**: 4686–703.
35. Moran JL and Posner JD. Phoretic self-propulsion. *Annu Rev Fluid Mech* 2017; **49**: 511–40.
36. Paxton WF, Kistler KC and Olmeda CC *et al.* Catalytic nanomotors: autonomous movement of striped nanorods. *J Am Chem Soc* 2004; **126**: 13424–31.
37. Van Haastert PJM. A stochastic model for chemotaxis based on the ordered extension of pseudopods. *Biophys J* 2010; **99**: 3345–54.
38. Merlitz H, Vuijk HD and Wittmann R *et al.* Pseudo-chemotaxis of active Brownian particles competing for food. *PLoS One* 2020; **15**: e0230873.
39. Pavlick RA, Sengupta S and McFadden T *et al.* A polymerization-powered motor. *Angew Chem Int Ed* 2011; **50**: 9374–7.
40. Ji Y, Lin X and Wu Z *et al.* Macroscale chemotaxis from a swarm of bacteria-mimicking nanoswimmers. *Angew Chem Int Ed* 2019; **58**: 12200–5.
41. Doney SC, Fabry VJ and Feely RA *et al.* Ocean acidification: the other CO_2 problem. *Annu Rev Mar Sci* 2009; **1**: 169–92.
42. Cuomo R, Sarnelli G and Savarese MF *et al.* Carbonated beverages and gastrointestinal system: between myth and reality. *Nutr Metab Cardiovas* 2009; **19**: 683–9.
43. Hall RA, De Sordi L and Maccallum DM *et al.* CO_2 acts as a signalling molecule in populations of the fungal pathogen candida albicans. *PLoS Pathog* 2010; **6**: e1001193.
44. Cummins EP, Selfridge AC and Sporn PH *et al.* Carbon dioxide-sensing in organisms and its implications for human disease. *Cell Mol Life Sci* 2014; **71**: 831–45.
45. Hall JE. *Guyton and Hall Textbook of Medical Physiology*, 13th edn. Philadelphia: Elsevier, 2015.
46. Zhan X, Wang J and Xiong Z *et al.* Enhanced ion tolerance of electrokinetic locomotion in polyelectrolyte-coated microswimmer. *Nat Commun* 2019; **10**: 3921.
47. Xu S, Li ZH and Wang Q *et al.* A novel one-step method to synthesize nano/micron-sized ZnO sphere. *J Alloy Compd* 2008; **465**: 56–60.
48. Whitman WG. The two film theory of gas absorption. *Int J Heat Mass Tran* 1962; **5**: 429–33.
49. Han J, Eimer DA and Melaaen MC. Liquid phase mass transfer coefficient of carbon dioxide absorption by water droplet. *Energy Procedia* 2013; **37**: 1728–35.